# Laser-intensity and wavelength dependence of mass-ablation rate, ablation pressure, and heat-flux inhibition in laser-produced plasmas

Faiz Dahmani and Tahar Kerdja
*Laboratoire Fusion, Centre de Developement des Technologies Avancées, Haut Commissariat à la Recherche, 2, Boulevard Frantz Fanon, Boîte Postale 1017 Alger-Gare, Algiers, Algeria*
(Received 30 October 1990)

Layered-target experiments at 1.06 $\mu$m have been performed in order to measure the mass-ablation rate $\dot{m}$ and ablation pressure $P_a$ as a function of absorbed laser intensity $I_a$ and wavelength $\lambda_L$ at irradiances of $10^{13}$–$10^{15}$ W/cm$^2$. The result can be put in the form $\dot{m}(\mathrm{kg/sec\,cm^2}) \simeq 143[I_a(\mathrm{W/cm^2})/10^{14}]^{1/3}[\lambda_L(\mu\mathrm{m})]^{-4/3}$ and $P_a(\mathrm{Mbar}) \simeq 11.9[I_a(\mathrm{W/cm^2})/10^{14}]^{2/3}[\lambda_L(\mu\mathrm{m})]^{-2/3}$. Hydrodynamical simulations using the code MEDUSA show heat-flux inhibition. This flux limitation is discussed in terms of a small lateral transport and the eventual presence of an intense magnetic field of order 0.76 MG.

## I. INTRODUCTION

Of great interest in laser fusion is the process of ablation. It is the source of driving pressure in the ablative compression of spherical targets, and, in particular, the source of its scaling with laser intensity and wavelength, which is of practical importance. Analytical expressions have been derived both for planar [1–4] and spherical [5–7] flows. On the other hand, several experiments have been carried out on the scaling of the mass-ablation rate and ablation pressure both for planar [8–14] and spherical [15–19] targets. Most of these results show that in planar targets the mass-ablation rate $\dot{m}$ and the ablation pressure scale as $I_a^{1/3}\lambda_L^{-4/3}$ and $I_a^{2/3}\lambda_L^{-2/3}$, respectively, for laser intensities higher than $10^{13}$ W/cm$^2$; whereas, for laser intensities below $10^{13}$ W/cm$^2$, the mass-ablation rate and the ablation pressure were found [20] to scale as $I_a^{5/9}\lambda_L^{-4/9}$ and $I_a^{7/9}\lambda_L^{-2/9}$, respectively. On the other hand, in spherical targets irradiated with 0.53- and 1.06-$\mu$m radiation, $\dot{m}$ and $P_a$ scale as $I_a^{0.7}$ and $I_a^{0.95}$, respectively, with little wavelength dependence.

In this paper, we present measurements of the mass-ablation rate and ablation pressure for planar aluminum targets driven by 1.06-$\mu$m laser light at intensities of $10^{13}$–$10^{15}$ W/cm$^2$. In order to also provide a scaling with wavelength and a normalization to previous data, we report measurements at 0.53 and 0.35 $\mu$m from Ref. [11]. We thus deduce two experimental relations for both the mass-ablation rate and ablation pressure with absorbed laser intensity $I_a$ and laser wavelength $\lambda_L$. In this work, the ablation pressure is deduced from the ablation rate and the absorbed laser intensity [4]. Our results indicate that both $\dot{m}$ and $P_a$ scale as $I_a^{1/3}\lambda_L^{-4/3}$ and $I_a^{2/3}\lambda_L^{-2/3}$, respectively.

We find that within the expected errors in normalization, the results given by our formulas are consistent with other reports on the mass-ablation rate [11,12] for 1.06, 0.53, and 0.35 $\mu$m and ablation pressure [11,13] for 1.06, 0.53, 0.35, and 0.27 $\mu$m at intensities beyond $10^{13}$ W/cm$^2$. Our study serves to extend the measurements for both $\dot{m}$ and $P_a$ to intensities higher than $10^{13}$ W/cm$^2$ for different wavelengths after the study that was done for laser intensities below $10^{13}$ W/cm$^2$ [20].

## II. EXPERIMENTAL CONDITIONS

The ablation measurements were obtained by irradiating planar targets with 700-psec duration [full width at half maximum (FWHM)] neodymium laser pulses of 1.06 $\mu$m at intensities of $10^{13}$–$10^{15}$ W/cm$^2$. Typical laser energies of up to 11 J were focused onto 44 $\mu$m (85% energy) using a 120-mm focal length quartz lens, and the effective aperture of the focused beam was $f/2$. The focal spot was controlled on every shot with an equivalent focal-plane-imaging system coupled to a video system. The pulse shape was measured with a high-speed streak camera and the energy with a Gentec calorimeter. The laser energy was varied to achieve different target intensities.

The targets were massive polyethylene ($CH_2$) foils with overcoatings of 0.26, 0.4, 0.44, and 0.7 $\mu$m aluminum, prepared by vacuum deposit. The uncertainty in the aluminum overlayer thickness, determined with a piezoelectric quartz, was less than 5%.

To determine the mass-ablation rate, several diagnostics were used: a luminosity time-of-flight spectrometer (LTOFS) for measurements of heat penetration in layered targets, a photomultiplier for soft-x-ray emission, and a Faraday-cup charge collector located at 45° from the target normal, to monitor the velocity of blowoff plasma. All the targets were irradiated at normal incidence.

Heat-penetration measurements using the LTOFS [21] were based on detecting the onset of emission of a C VI line (3434 Å) in the plasma ablated from the $CH_2$ target as the laser intensity was increased. Since the upper level is populated through electronic recombination of $C^{6+}$ ions, spectrally and spatially resolved emission from the outer coronal plasma region samples the time-of-flight distribution of $C^{6+}$ ions. Observations were made using a 1.05-m monochromator at a distance of $\geq 5$ mm from the target surface to avoid the effects of Stark broadening and self-absorption in the C VI line. Light emission at 3434 Å from a pure aluminum target was found to be

 

negligibly small throughout the laser intensity range of the experiment.

An x-ray yield detector consisting of a scintillator photomultiplier combination coupled with light tight aluminized foils [20–22] (cutoff energy $\simeq 2$ keV) was used to measure the x-ray-emission intensity from the plasma.

A Faraday-cup charge collector was used at an angle of 45° from the target normal to obtain the ion blowoff velocities. The Faraday cup was a quite deep copper cylindrical cup placed behind a pair of grids, one of which was based at $-350$ V and the other kept at ground potential. The background pressure in the target chamber during all these measurements was maintained at approximately $3\times10^{-5}$ Torr.

## III. EXPERIMENTAL RESULTS

The variation of ion peak (corresponding to the flight time at maximum in the Faraday-cup signal) expansion velocity as a function of absorbed laser intensity for the 0.4-$\mu$m-aluminum-layered target is shown in Fig. 1. It is observed that ion pic velocities from the layered target correspond to those from the bare aluminum target for low laser intensities. As the laser intensity is increased, carbon ions start appearing. The corresponding value of the laser intensity is noted to be the ablation intensity for the overlayer thickness (this value in the case of the 0.4-$\mu$m-aluminum-layered target is $\simeq 1.14\times10^{14}$ W/cm$^2$).

These observations were further verified by measuring the x-ray-emission intensity transmitted through aluminized foils. The variation of this x-ray intensity as a function of laser intensity for polyethylene, aluminum, and 0.4-$\mu$m-aluminum-layered targets is shown in Fig. 2. Since aluminum is a higher-$Z$ material, the x-ray intensity from the aluminum target is higher than that for a polyethylene target. The x-ray intensity for the layered target coincides with that for a pure aluminum target at smaller laser intensities and starts deviating from it at higher laser intensities. The value of the laser intensity where the x-ray intensity from the layered target starts differing from that for the pure aluminum target is noted to be the value for which the ablation of the overlayer occurs.

The variation of peak C VI line intensity as a function of laser intensity for the 0.4-$\mu$m-aluminum-layered target is shown in Fig. 3. The signal for the bare $CH_2$ target is also shown in Fig. 3 for comparison. It is seen that for the case of the layered target, the C VI line signal begins to appear when the laser intensity is increased beyond

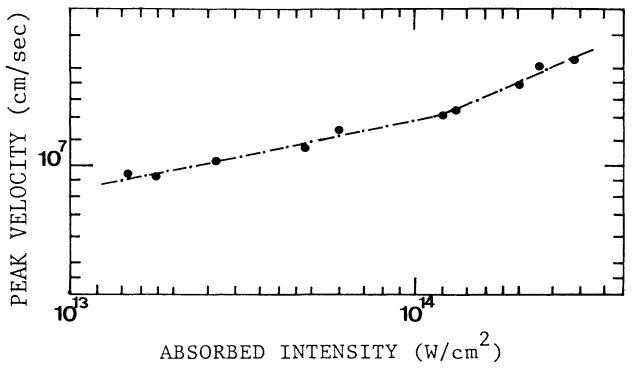


FIG. 1. Variation of ion peak expansion velocity with absorbed laser intensity for the aluminum-layered target.

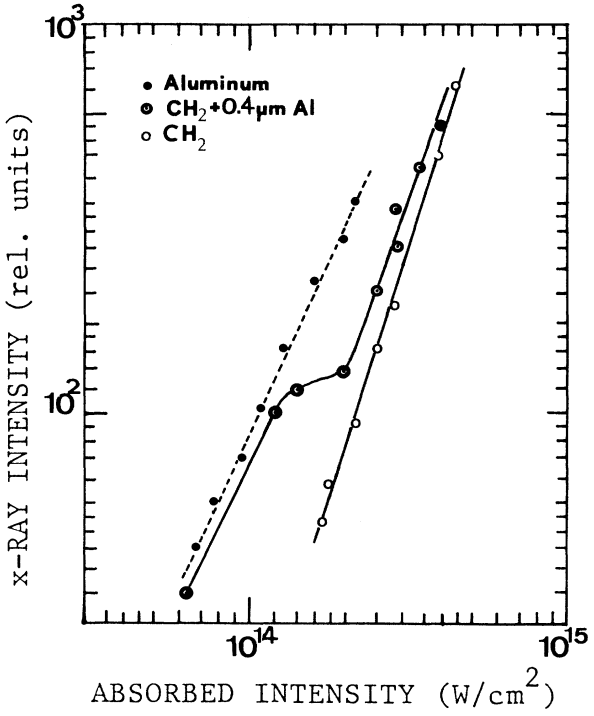


FIG. 2. Variation of x-ray intensity for aluminum, polyethylene, and aluminum-overlayered targets as a function of absorbed laser intensity.

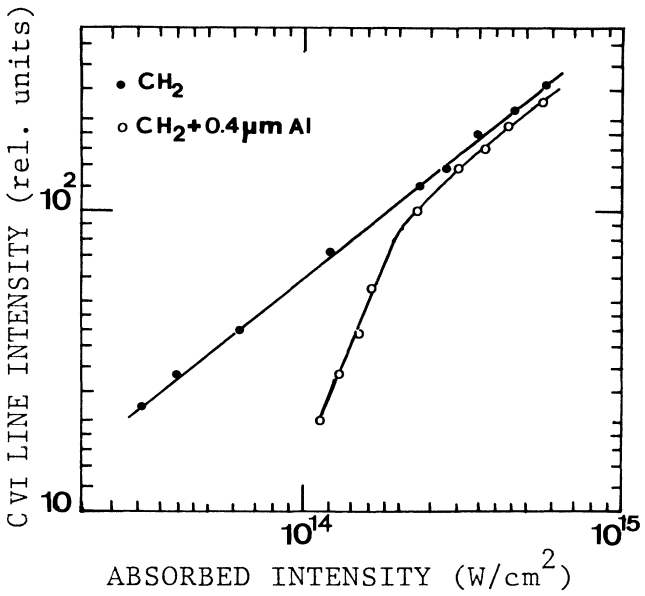


FIG. 3. Variation of C VI 3434-Å line intensity as a function of absorbed laser intensity for bare polyethylene and aluminum-layered targets.

$1.14\times10^{14}$ W/cm$^2$. Laser intensities required to ablate thicknesses of 0.26, 0.34, 0.44, and 0.7 $\mu$m of aluminum, determined in the same manner, are $2.9\times10^{13}$, $2.9\times10^{14}$, $10^{14}$, and $8\times10^{14}$ W/cm$^2$, respectively.

In Table I we give an example of the characteristic overlayer thicknesses $d_T$ ablated experimentally by using the LTOFS diagnostic for 1.06-$\mu$m laser light. Data for 0.53- and 0.35-$\mu$m laser light from Ref. [11] are also represented. The last column of Table I represents the value of $A$ defined as

$$A=(\rho_0 d_T)/(I_a^{1/3}\lambda_L^{-4/3}\tau_L) .$$

One can see that for our various experimental conditions, $A$ is constant with a value of $0.32\pm0.03$.

If we define the mass-ablation rate $\dot{m}$ as $\dot{m}=(\rho_0 d_T)/\tau_L$, $\rho_0$ being the solid density of the overlayer thickness, and taking into account the definition of $A$, we obtain the experimental mass-ablation rate $\dot{m}$ kg/sec cm$^2$ in

$$\dot{m}_{\text{expt}}\simeq 143\left[\frac{I_a}{10^{14}}\right]^{1/3}[\lambda_L(\mu\text{m})]^{-4/3} , \quad (1)$$

where $I_a$ is in W/cm$^2$.

In the assumption of steady-state planar geometry, the ablation pressure can be deduced directly from the conservation of momentum and is given by the mass-ablation rate and the absorbed intensity. In that assumption, the ablation pressure is $P_a=(\dot{m}I_a)^{1/2}$.

We can thus obtain from Eq. (1) the experimental ablation pressure in Mbar:

$$P_a\simeq 11.9\left[\frac{I_a}{10^{14}}\right]^{2/3}[\lambda_L(\mu\text{m})]^{-2/3} . \quad (2)$$

Figures 4 and 5 show the mass-ablation rate and the ablation pressure, respectively, as a function of absorbed laser intensity for different laser wavelengths.

TABLE I. Experimental values of characteristic overlayer thicknesses $d_T$ as a function of absorbed intensity $I_a$, wavelength $\lambda_L$, and pulse width $\tau_L$. In the last column, we have reported $A=[\rho_0(\text{g cm}^{-3})][d_T(\text{Å})]/[I_a(\text{W/cm}^2)]^{1/3}[\lambda_l(\mu\text{m})]^{-4/3}[\tau_L(\text{nsec})]$. The values at 0.53- and 0.35-$\mu$m laser light (denoted by the asterisk) have been reported by Key *et al.* (Ref. [11]).

| $\lambda_L$ ($\mu$m) | $\tau_L$ (nsec) | $I_a$ (W/cm$^2$) | $d_T$ ($\mu$m) | $A$ |
|---|---|---|---|---|
| 1.06 | 0.7 | $2.9\times10^{13}$ | 0.26 | 0.35 |
| | | $\times10^{14}$ | 0.34 | 0.30 |
| | | $1.14\times10^{14}$ | 0.40 | 0.34 |
| | | $2\times10^{14}$ | 0.44 | 0.31 |
| | | $8\times10^{14}$ | 0.70 | 0.31 |
| 0.53* | 1 | $3\times10^{14}$ | 2 | 0.34 |
| | | $1.8\times10^{15}$ | 3.33 | 0.32 |
| 0.35* | 1 | $1.8\times10^{14}$ | 2.59 | 0.31 |
| | | $1.8\times10^{15}$ | 5.93 | 0.32 |

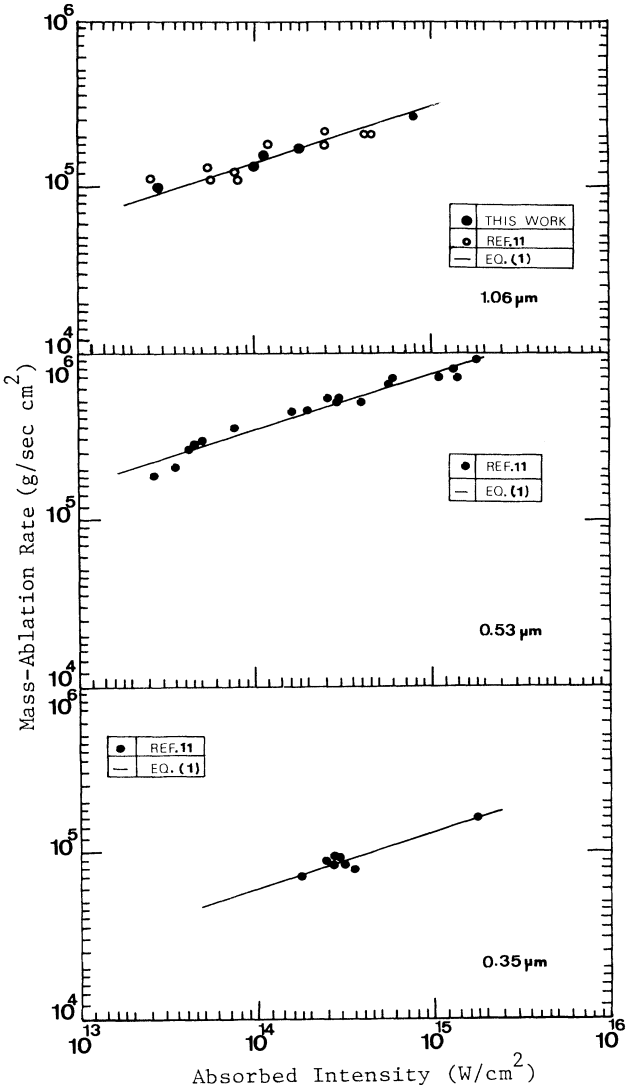


FIG. 4. Comparison of measured mass-ablation rate from (a) Ref. [11] and present work for $\lambda_L=1.06$ $\mu$m (open and solid circles), (b) Ref. [11] for $\lambda_L=0.53$ $\mu$m (solid circles), and (c) Ref. [11] for $\lambda_L=0.35$ $\mu$m (solid circles) with the experimental relation Eq. (1) (solid lines).

## IV. COMPARISON WITH NUMERICAL SIMULATIONS

We have used the Lagrangian hydrodynamics code MEDUSA, developed by Christiansen, Ashby, and Roberts [23], to check the validity of the principal results in our experimental work, and to evaluate the range of applicability of our experimental relations [Eqs. (1) and (2)]. It is a one-dimensional Lagrangian hydrodynamics code, and was used here in plane geometry with a perfect-gas equation of state for ions and the Thomas-Fermi equation of state (with modified corrections to give correct solid density) for electrons.

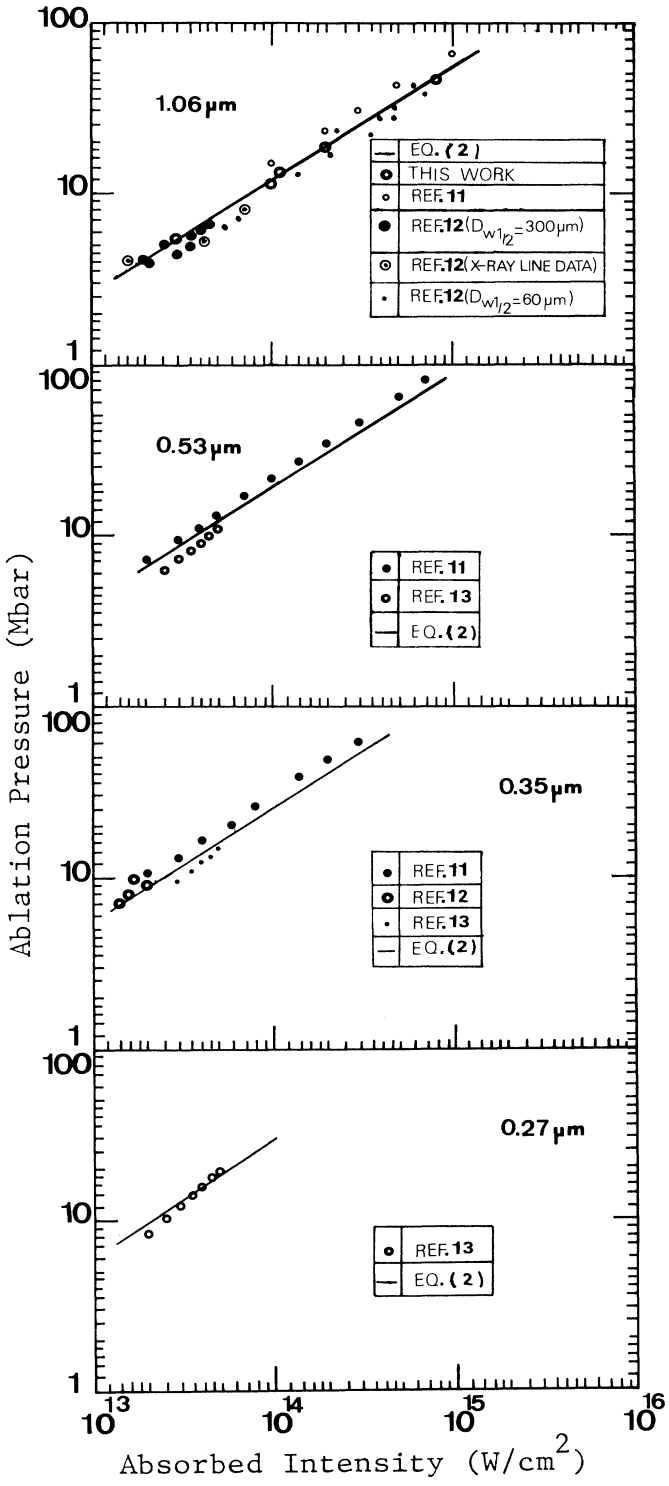


FIG. 5. Comparison of ablation pressure from (a) Refs. [11], [12], and present work for $\lambda_L = 1.06$ $\mu$m (open and solid circles), (b) Refs. [11] and [13] for $\lambda_L = 0.53$ $\mu$m (open and solid circles), (c) Refs. [11—13] for $\lambda_L = 0.35$ $\mu$m (open and solid circles), and (d) Ref. [13] for $\lambda_L = 0.27$ $\mu$m (open circles) with the experimental relation Eq. (2) (solid lines).

The comparison of our picosecond experiments at 1.06 $\mu$m with hydrodynamic simulation allows us to determine the usual flux limit factor $F$. On the other hand, solutions of the Fokker-Planck equations indicated the presence of nonlocal transport and were well fitted with hydrocodes that use the harmonic method of computing the "effective conductivity" using a flux limiter $F$ between 0.06 and 0.1 [24]. An analytical solution of the Fokker-Planck equations was proposed in the form of a delocalized flux model; the heat flux obtained was well fitted by the macroscopic formula [25,26]

$$Q(x) = \int_{-\infty}^{+\infty} W(x,x') Q_{\mathrm{SH}}(x') dx' ,$$

where $Q_{\mathrm{SH}}(x')$ is the Spitzer-Härm heat flux at $x'$ and the kernel $W(x,x')$ has the exponential form

$$W(x,x') = -\frac{1}{2\lambda(x')} \exp\left[ -\frac{|x-x'|}{\lambda(x')} \right] ,$$

where $\lambda(x')$ is the delocalization mean free path at $x'$ and is much larger than the electron mean free path $\lambda_0$ because the electrons involved in the thermal transport have several times the thermal velocity [26].

The use of the above model in the hydrodynamic codes cannot be made directly. To do that, we have to introduce for the inverse bremsstrahlung absorption in the corona a similar delocalized model [27], which leads from the viewpoint of the temperature, the temperature gradient, and the ablation pressure at the front of the maximum temperature to results similar to those obtained with a harmonic law using a factor of flux limiter $F \leq 0.1$ [27]. Therefore, at the ablation front, the delocalized formula leads to a fit, which can only influence the hydrodynamic instabilities.

In the code MEDUSA, thermal heat flux is limited to the free-flux limit value defined by $(\frac{1}{4})(F n_e v_e k T_e)$, where $F$ is an adjustable numerical constant. Suprathermal electron transport is described by a multigroup treatment [23] (ten groups of fast electrons are used); in contrast to the thermal transport, they are classically treated without any flux limiter. Energy is absorbed by inverse bremsstrahlung absorption and 20% of the energy reaching the critical density is dumped into fast electrons with a hot-electron temperature $T_H$, which is measured experimentally.

Details of the algorithms and physics used in MEDUSA may be found in Ref. [23].

To establish conditions similar to those used in the experiment, we used a constant-intensity laser pulse, having a long enough pulse length to produce steady-state conditions in the plasma flow. The energy was deposited at the critical surface.

An example of the comparison described above is shown in Fig. 6, where it is plotted as function of the flux limit factor $F$, the corresponding normalized value of $d_T$. In that case, for $I_{\mathrm{abs}} \simeq 2 \times 10^{14}$ W/cm$^2$ and $\lambda_L = 1.06$ $\mu$m, $T_H$ was taken as 1.4 keV [curve (a)]. In order to check the efficiency of fast-electron transport in this case, we dumped their energy into the thermal electrons at critical density [curve (b)]: the small difference of the two

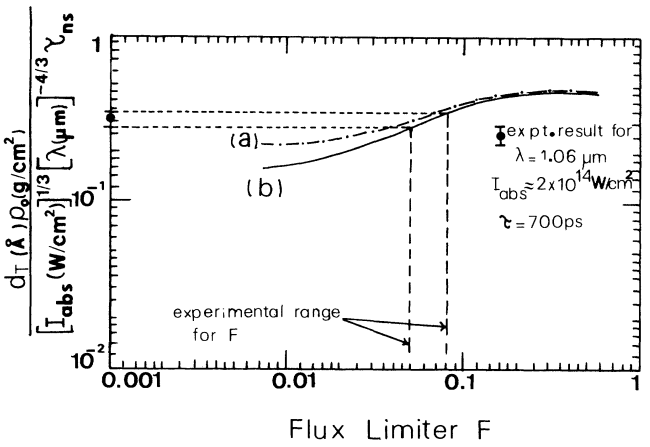


FIG. 6. Results of the simulations of the normalized values of $d_T$ as a function of the flux limiter $F$ for the experimental conditions given in the inset. We used inverse bremsstrahlung absorption, and 20% of the energy reaching critical density is dumped into fast electrons with $T_H = 1.4$ keV [curve (a)] or into thermal electrons [curve (b)]. ● represents experimental value of $A$ with corresponding error bars.

curves shows that, with these conditions, suprathermal transport is negligible. This was expected due to the faster thermalization rate at this low hot-electron temperature. Experimentally, this point is confirmed by the observation of a negligible fraction of absorbed energy in fast ions. Consequently, taking into account the experimental uncertainties, the flux limiter $F$ for the thermal population is such that $0.05 \leq F \leq 0.08$.

## V. DISCUSSION

In these experiments, energy absorption by the target is almost complete (since the measurements of the reflected energy in the specular direction show that about 80% of the incident laser energy is absorbed), indicating that inverse bremsstrahlung absorption is the dominant mechanism. The fluid flow in the ablation region is one dimensional and planar, since the ion velocity distribution functions represented for all layered targets used here showed that clearly. This ablative flow is matched onto the plasma rarefaction in the corona of the target. In general, the density gradient length $L$ of the underdense plasma is of the order of $C_s\tau_L$ [2], where $C_s$ is the acoustic speed at the absorption surface. In these experiments, this is typically 100 $\mu$m. However, spherical divergence will limit this scale length to approximately the spot diameter of $D \simeq 44$ $\mu$m [2]. In this case $C_s\tau_L$ exceeds the focal spot diameter $D$; the expansion is no longer planar, without being completely spherical. Yet, the asymptotic condition for a spherical flow ($C_s\tau_L \gg D$) is not satisfied.

As suggested by some authors [28,29], the ion energy distribution consists of two parts: an early phase and a latter phase. In the early-phase heating, the plasma expansion takes place when lateral conduction is yet not prominent and the corresponding ions appear as if the target ablation area is equal to the focal spot area. The latter-phase heating produces relatively cooler plasma because the lateral transport takes over during the heating. When the lateral spread energy is small, the ions from the early phase dominate the distribution (that is what the charge collector signal shows in our case). But, when the lateral spread energy is important, the ions of the latter phase start dominating in number, causing a deviation in the ion energy scaling with laser intensity.

Evidence of an eventual lateral energy transport is an increase with laser intensity of the velocity fraction $\Delta v/v_p$ [29], where $v_p$ is the peak velocity and $\Delta v$ is the velocity corresponding to the flight time at half maximum in the Faraday-cup signal. The value $\Delta v/v_p$ was measured as a function of laser intensity for laser intensities higher than those necessary for the ablation of the several layered targets used here and was found to be constant ($\Delta v/v_p \simeq 1.92 \pm 0.08$ in the case of $CH_2 + 0.4\mu$m Al.)

Furthermore, for all layered targets used here, the comparison between the x-ray-intensity curves for layered and pure polyethylene targets for laser intensities higher than those corresponding to the ablation of the layered targets showed that the difference of the x-ray intensities is somewhat different of the x-ray-intensity value at the ablation. An example of a such comparison is given in Table II for $CH_2 + 0.4$-$\mu$m-Al targets (see Fig. 2). From Table II we see that $\Delta$ (x ray) is more or less constant, which means that the same quantity of aluminum matter is ablated for any laser intensity beyond that corresponding to the ablation. This result with the above one leads us to conclude, that if there is lateral conduction, it can only be small and therefore negligible to compromise the expansion of the plasma.

We have shown that the agreement of the experimental results with numerical simulations requires a flux limiter $F$ between 0.05 and 0.08. These values are somewhat lower than those expected for a delocalized heat flux ($F \simeq 0.1$) [24–27]. This difference cannot be explained by the method used in the code MEDUSA to calculate the effective thermal flux. They may be due to the presence of magnetic fields and/or to the fact that electrons responsible for part of the heat transport are convected out of the laser spot to the surrounding material. This flux limitation is characterized by the fact that the thermal

TABLE II. The x-ray intensity values for $CH_2$ and $CH_2 + 0.4$-$\mu$m-Al targets (in relative units) as a function of laser intensity. The last column gives the differences between x-ray-intensity values of $CH_2$ and $CH_2 + 0.4$-$\mu$m-Al targets, i.e., the quantity of x rays emitted from the aluminum.

| $I_a$ (W/cm$^2$) | X-ray intensity | | |
|---|---|---|---|
| | $CH_2$ | $CH_2 + 0.4$ $\mu$m Al | $\Delta$(x rays) |
| $1.14 \times 10^{14}$ | | 120 (ablation) | |
| $3 \times 10^{14}$ | 300 | 420 | 120 |
| $3.5 \times 10^{14}$ | 660 | 530 | 130 |
| $4 \times 10^{14}$ | 950 | 820 | 130 |

heat flux conducted toward the overcritical zones represents only a fraction of the absorbed energy; the mass-ablation rate associated is consequently low. We examine now several possibilities that can explain these differences. Until now, there has been no direct link between any flux limitation and the setup of instabilities such as ion acoustic or electromagnetic instabilities (Weibel instabilities), although the strong turbulence of the latter ones in the corona is now recognized by several authors.

The existence of the bidimensional effects represents an important aspect in the interpretation of the different transport processes. Effectively, the absorbed energy cannot only spread in the axial direction, but also laterally, which represents a loss in the heat transport. There are two types of lateral energy losses: the first results from the decoupling of the conduction electrons (suprathermal electrons) at the critical surface and below. These electrons, which are collisionless, can orbit around the azimuthal magnetic field and can be deposited in the cold part of the target [30]; the resulting reduction in the populations of conducting electrons results in a lower axial thermal flux. However, we are sure that the fraction of energy conducted by these electrons in our experiments is negligible because of their low temperature $T_H$ and their fast thermalization around the critical surface. The second type of lateral losses is by thermal conduction. We cannot exclude completely the eventuality of a broadening of the focal spot resulting from the natural lateral plasma spreading even for short laser pulses. Effectively, we have seen above that the plasma expansion is not completely planar. This result can lead to a low effective laser intensity. On the other hand, this effect, as shown above, is not important and cannot reduce itself the flux limiter to the range of $0.05 \leq F \leq 0.08$. Therefore, we suppose that second process characterized by the presence of intense magnetic fields produced by the $\nabla n_e \times \nabla T_e$ sources near the edge of the laser beam can necessarily reduce the axial thermal transport [31,32]. Effectively, magnetic fields of the order of 1 MG in the corona have been measured experimentally [33]. A simple saturation mechanism for the field has been considered by Max, Manheimer, and Thomson [34] and gives a saturated field magnitude, in MG of

$$B \simeq 3.3 (T_e)^{1/2} \left[ \frac{10}{L} \right] \left[ \frac{A}{Z+1} \right]^{1/2} ,$$

with $T_e$ in keV and $L$ in $\mu$m. For reasonable parameters $T_e = 520$ eV (deduced from the charge collector), $A/Z = 2$, and $L = 44$ $\mu$m ($= 2R$), the magnetic field is calculated to be $B \simeq 0.76$ MG.

The effect of magnetic fields on the thermal conductivity has been calculated by Braginskii [35] by a method similar to that of Spitzer. In the presence of a noncollinear temperature gradient $\nabla T_e$ to **B**, the heat flux has been given under a tensorial form [35]:

$$\mathbf{q} = -K_0 \nabla T_e - K_\perp \nabla_\perp T_e - K_\alpha (\mathbf{h} \times \nabla T_e) .$$

In this expression, $\nabla T_e$ and $\nabla_\perp T_e$ represent, respectively, the parallel and perpendicular components of the thermal gradient to the magnetic field. It seems that $K_0$ [4], the parallel conductivity, is not modified by **B**. On the other hand, $K_\perp$ and $K_\alpha$ depend on $B$ by the following relations [35]:

$$K_\perp = K_0 \left[ \frac{\epsilon_1' x^2 + \epsilon_0'}{\epsilon_0' (x^4 + \delta_1 x^2 + \delta_0)} \right] ,$$

$$K_\alpha = K_0 \frac{x(\epsilon_1'' x^2 + \epsilon_0'')}{\epsilon_0 (x + {}^4\delta_1 \times + {}^2\delta_0)} .$$

In these expressions, $\epsilon_0$, $\delta_0$, $\delta_1$, $\epsilon_0'$, $\epsilon_1'$, $\epsilon_0''$, and $\epsilon_1''$ are coefficients close to unity and depend only on $Z$ [35]. While $x = \Omega \tau_{ei}$, $\Omega = eB/m_e c$ is the electron gyrofrequency and $\tau_{ei}$ is the electron-ion collision time [36,37]. Taking into account the expressions of $\Omega$ and $\tau_{ei}$, we get for $x$

$$x \simeq \frac{190}{Z} B T_e^{3/2} \left[ \frac{n_e}{10^{21}} \right]^{-1} ,$$

with $n_e$ in cm$^{-3}$. Note the very strong dependence on electron temperature $T_e$ and electron density $n_e$.

When $x \gg 1$, we can have $K_\perp \simeq K_0/x^2$. Therefore, for $T_e = 520$ eV, $B \simeq 0.76$ MG, $n_e = n_c = 10^{21}$ cm$^{-3}$, and $Z = 13$, we obtain $x = 4.2$, which gives $K_\perp/K_0 \simeq 0.056$. Note the agreement of this value with our flux limitation range $0.05 \leq F \leq 0.08$.

Our reported experimental relations [Eqs. (1) and (2)] are both in very good agreement with the results of Refs. [11], [12], and [13] for laser wavelengths $\lambda_L = 1.06$, 0.53, 0.35, and 0.27 $\mu$m and laser intensities higher than $10^{13}$ W/cm$^2$ (Figs. 4 and 5). In Ref. [13], the ablation pressure is much smaller than that of our result [Eq. (2)] for laser intensities lower than $10^{13}$ W/cm$^2$. This can be explained by the fact that at these intensities the laser energy is no longer absorbed in the vicinity of the critical density $n_c$ but rather at a density $n_1 < n_c$ [20,36]. This situation leads to a change in the scaling with absorbed laser intensity and wavelength: $P_a \propto I_a^{7/9} \lambda_L^{-2/9}$ [20,36].

## VI. CONCLUSIONS

We have measured the ablation rate in planar targets irradiated by 1.06-$\mu$m laser light. We have put our results in the form given by Eqs. (1) and (2), which is in very good agreement with the data of others.

Our results are also in good agreement with hydrodynamic simulations using the code MEDUSA for a flux limiter $F$ in the range of $0.05 \leq F \leq 0.08$. To explain this flux limitation, we have seen that the nonlocal nature of the thermal electron transport was incapable itself of taking into account this flux limitation. Effectively, this nonlocal theory does not take into account the direct or indirect effects of intense magnetic fields and/or lateral

spreading on the axial thermal transport. That is why we have supposed that both the small lateral conduction present in this experiment, despite the one-dimensional expansion and an eventual presence of a magnetic field of the order of 0.76 MG in the corona, can match well the flux limitation range obtained here.

## ACKNOWLEDGMENTS

The authors wish to thank D. Ghobrini and S. Malek for their technical assistance. One author (F.D.) would like to thank Dr. Hall and Dr. Djaoui for their helpful discussions and the facility to use MEDUSA during his stay at the University of Essex (United Kingdom).

[1] A. Caruso and R. Gratton, Plasma Phys. **10**, 867 (1968).
[2] P. Mora, Phys. Fluids **25**, 1051 (1982).
[3] W. M. Manheimer, D. G. Colombant, and J. H. Gardner, Phys. Fluids **25**, 1644 (1982).
[4] R. Fabbro, C. E. Max, and E. Fabre, Phys. Fluids **28**, 1463 (1985).
[5] R. E. Kidder, Nucl. Fusion **8**, 3 (1968).
[6] S. J. Gitomer, R. L. Morse, and B. S. Newberger, Phys. Fluids **20**, 244 (1977).
[7] C. E. Max, C. G. McKee, and W. C. Mead, Phys. Fluids **23**, 1620 (1980).
[8] F. Amiranoff, R. Fabbro, E. Fabre, C. Garban-Labaune, J. Virmont, and M. Weinfeld, Phys. Rev. Lett. **43**, 522 (1979); R. Fabbro, E. Fabre, F. Amiranoff, C. Garban-Labaune, J. Virmont, M. Weinfeld, and C. E. Max, Phys. Rev. A **26**, 2289 (1982).
[9] B. Yaakobi, T. Boehly, P. Bourke, Y. Conturie, R. S. Craxton, J. Delettrez, J. M. Forsyth, R. D. Frankel, L. M. Goldman, R. L. McCrory, M. C. Richardson, W. Seka, D. Shvarts, and J. M. Soures, Opt. Commun. **39**, 175 (1981).
[10] H. Nishimura, H. Azechi, K. Yamada, A. Tamura, Y. Inada, F. Matsuoka, H. Hamada, Y. Suzuki, S. Nakai, and C. Yamanaka, Phys. Rev. A **23**, 2011 (1981).
[11] M. H. Key, W. T. Toner, T. J. Goldsack, J. D. Kilkenny, S. A. Veats, P. F. Cunningham, and C. L. S. Lewis, Phys. Fluids **7**, 2011 (1983).
[12] B. Meyer and G. Thiell, Phys. Fluids **27**, 302 (1984).
[13] A. Ng, D. Pasini, P. Celliers, D. Parfeniuk, L. DaSilva, and J. Kwan, Appl. Phys. Lett. **45**, 1046 (1984).
[14] T. Boehly, K. A. Tanaka, T. Mochizuki, and C. Yamanaka, J. Appl. Phys. **60**, 3840 (1986).
[15] T. J. Goldsack, J. D. Kilkenny, B. J. McGowan, P. F. Cunningham, C. L. S. Lewis, M. H. Key, and P. T. Rumsby, Phys. Fluids **25**, 1634 (1982).
[16] B. Yaakobi, J. Delettrez, L. M. Goldman, R. L. McCrory, R. Majoribanks, M. C. Richardson, D. Shvarts, S. Skupsky, J. M. Soures, C. Verdon, D. M. Villeneuve, T. Boehly, R. Hutchinson, and S. Letzring, Phys. Fluids **27**, 516 (1984).
[17] B. Yaakobi, O. Barnouin, J. Delettrez, L. M. Goldman, R. Majoribanks, R. L. McCrory, M. C. Richardson, and J. M. Soures, J. Appl. Phys. **57**, 4354 (1984).
[18] T. Yamanaka, T. Mochizuki, H. Azechi, H. Nishimura, M. Yamanaka, M. Miyanaga, H. Niki, E. Fujiwara, H. Shiraga, K. Okada, S. Sakabe, Y. Kato, Y. Kitagawa, M. Nakatsuka, K. Mima, N. Nishihara, T. Yabe, S. Nakai, and C. Yamanaka, Laser Part. Beams **4**, 43 (1985).
[19] E. Fabre, C. Garban-Labaune, R. Fabbro, B. Faral, A. Michard, H. Pepin, A. Poquerusse, J. Virmont, F. Briand, J. Briand, P. Mora, J. F. Luciani, R. Pellat, H. Baldis, F. Cottet, and J. P. Romain, IAEA Report No. CN-44/B-III-4, 1984 (unpublished).
[20] F. Dahmani and T. Kerdja, Laser Part. Beams (to be published).
[21] T. Kerdja, F. Dahmani, and D. Ghobrini, Laser Part. Beams (to be published).
[22] K. Eidmann, M. H. Key, and R. Sigel, J. Appl. Phys. **47**, 2402 (1976).
[23] J. P. Christiansen, D. E. T. F. Ashby, and K. V. Roberts, Comput. Phys. Commun. **7**, 271 (1974).
[24] J. P. Matte, T. W. Johnston, J. Delettrez, and R. L. McCrory, Phys. Rev. Lett. **53**, 1461 (1984).
[25] J. F. Luciani, P. Mora, and J. Virmont, Phys. Rev. Lett. **51**, 1664 (1983).
[26] J. Delettrez, Can. J. Phys. **64**, 932 (1986).
[27] J. F. Luciani, P. Mora, and R. Pellat, Phys. Fluids **28**, 835 (1986).
[28] H. C. Pant, S. Sharma, L. J. Dhareshwar, and P. A. Naik, *Proceedings of the 1983 College on Plasma Physics, Trieste, Italy,* edited by McNamara (World Scientific, Singapore, 1984).
[29] M. H. Key, Rutherford Appleton Laboratory Annual Report 1981, Chap. 4 (unpublished).
[30] M. A. Yates, D. B. Van Hulsteyn, H. Rutkowski, G. Kyrala, and J. U. Brackbill, Phys. Rev. Lett. **49**, 1702 (1982).
[31] J. A. Stamper, K. Papadopoulos, R. N. Sudan, S. O. Dean, E. A. McLean, and J. M. Dawson, Phys. Rev. Lett. **26**, 1012 (1971).
[32] R. S. Craxton and M. G. Haines, Phys. Rev. Lett. **35**, 1336 (1975).
[33] A. Raven, O. Willi, and P. T. Rumsby, Phys. Rev. Lett. **41**, 554 (1978).
[34] C. E. Max, W. M. Manheimer, and J. J. Thomson, Phys. Fluids **21**, 128 (1978).
[35] S. J. Braginskii, *Review of Plasma Physics* (Consultants Bureau, New York, 1966).
[36] F. Dahmani and T. Kerdja, Phys. Fluids B (to be published).
[37] C. E. Max (unpublished).